Atheroma Susceptible to Thrombosis Exhibit Impaired Endothelial Permeability In Vivo as Assessed by Nanoparticle-Based Fluorescence Molecular Imaging

Ashley F. Stein-Merlob, MD; Tetsuya Hara, MD, PhD; Jason R. McCarthy, PhD; Adam Mauskapf, BS; James A. Hamilton, PhD; Vasilis Ntziachristos, PhD; Peter Libby, MD; Farouc A. Jaffer, MD, PhD

Background—The role of local alterations in endothelial functional integrity in atherosclerosis remains incompletely understood. This study used nanoparticle-enhanced optical molecular imaging to probe in vivo mechanisms involving impaired endothelial barrier function in experimental atherothrombosis.

Methods and Results—Atherosclerosis was induced in rabbits (n=31) using aortic balloon injury and high-cholesterol diet. Rabbits received ultrasmall superparamagnetic iron oxide nanoparticles (CLIO) derivatized with a near-infrared fluorophore (CyAm7) 24 hours before near-infrared fluorescence imaging. Rabbits were then either euthanized (n=9) or underwent a pharmacological triggering protocol to induce thrombosis (n=22). CLIO-CyAm7 nanoparticles accumulated in areas of atheroma (P<0.05 versus reference areas). On near-infrared fluorescence microscopy, CLIO-CyAm7 primarily deposited in the superficial intima within plaque macrophages, endothelial cells, and smooth muscle cells. Nanoparticle-positive areas further exhibited impaired endothelial barrier function as illuminated by Evans blue leakage. Deeper nanoparticle deposition occurred in areas of plaque neovascularization. In rabbits subject to pharmacological triggering, plaques that thrombosed exhibited significantly higher CLIO-CyAm7 accumulation compared with nonthrombosed plaques (P<0.05). In thrombosed plaques, nanoparticles accumulated preferentially at the plaque-thrombus interface. Intravascular 2-dimensional near-infrared fluorescence imaging detected nanoparticles in human coronary artery–sized atheroma in vivo (P<0.05 versus reference segments).

Conclusions—Plaques that exhibit impaired in vivo endothelial permeability in cell-rich areas are susceptible to subsequent thrombosis. Molecular imaging of nanoparticle deposition may help to identify biologically high-risk atheroma. **(*Circ Cardiovasc Imaging*. 2017;10:e005813. DOI: 10.1161/CIRCIMAGING.116.005813.)**

Key Words: atherosclerosis ■ cholesterol ■ endothelium ■ molecular imaging ■ thrombosis

The majority of acute coronary syndrome results from focal thrombosis complicating atherosclerotic plaques. Achieving an understanding of rupture of the plaque's fibrous cap has dominated thinking about the underlying mechanisms of coronary thrombosis.[1] However, postmortem human studies of coronary vessels by histology have found that the majority of plaques with thin fibrous caps did not disrupt.[2] Furthermore, plaque rupture is diminishing as a cause of acute coronary syndrome, likely due to statin treatment and other preventive measures. Therefore, alterations in endothelial functions merit further scrutiny, particularly given the dearth of mechanistic information about the mechanisms of superficial erosion and subsequent plaque thrombosis.[3] Although many studies have addressed endothelial vasodilator function in vivo, investigation of other aspects of local endothelial integrity and its role in atherothrombosis has lagged.

See Editorial by Calcagno and Fayad
See Clinical Perspective

This study tested the hypothesis that plaques exhibiting impaired in vivo endothelial barrier function (abnormal permeability) would be predisposed to plaque thrombosis. We further hypothesized that plaque susceptibility to thrombosis would relate to areas of high atheroma cell density, as plaque cells are often proinflammatory and can amplify endothelial cell dysfunction.[4] To test these hypotheses, we engineered and applied CLIO-CyAm7, a near-infrared fluorophore–derivatized ultrasmall superparamagnetic iron oxide (USPIO) nanoparticle,

Received October 25, 2016; accepted March 28, 2017.

From the Cardiovascular Research Center, Cardiology Division (A.F.S., T.H., A.M., F.A.J.) and Center for Systems Biology (J.R.M.), Department of Cardiology, Massachusetts General Hospital, Harvard Medical School, Boston; Department of Physiology and Biophysics, Boston University School of Medicine, MA (J.A.H.); Department of Biomedical Engineering, Boston University, MA (J.A.H.); Institute of Biological and Medical Imaging, Chair of Biological Imaging, Technical University of Munich, Germany (V.N.); and Cardiovascular Division, Brigham and Women's Hospital, Harvard Medical School, Boston, MA (P.L.).

Guest Editor for this article was Marc R. Dweck, MD, PhD.

The Data Supplement is available at http://circimaging.ahajournals.org/lookup/suppl/doi:10.1161/CIRCIMAGING.116.005813/-/DC1.

Correspondence to Farouc Jaffer, MD, PhD, MGH CVRC, 185 Cambridge St, Simches Research Bldg, Room 3206, Boston, MA 02114. E-mail fjaffer@mgh.harvard.edu

to assess experimental atherosclerosis biology in vivo. We first assessed the cellular distribution of the fluorescent USPIO in rabbit atheroma and found that its cellular targeting profile appeared diffusion limited. This finding motivated us to investigate whether an impaired endothelial barrier function might govern CLIO-CyAm7 nanoparticle deposition into atheroma. Next, to understand the relationship between nanoparticle deposition and plaque thrombosis, we used a modified procedure developed by Constantinides to trigger thrombosis[5–7] to assess whether sites of mural thrombosis accumulated CLIO-CyAm7. Finally, we analyzed the ability of CLIO-CyAm7 nanoparticles to enable intravascular near-infrared fluorescence (NIRF) molecular imaging of impaired endothelial barrier function in vivo in coronary artery-sized vessels.

Methods

Materials and Methods are available in the online-only Data Supplement.

Animal Model of Atherothrombosis

Animal protocols were approved by the Massachusetts General Hospital Subcommittee on Research Animal Care. New Zealand white rabbits (n=31) consumed a high-cholesterol diet for 2 weeks before abdominal aortic balloon injury followed by 6 weeks of 1% high-cholesterol diet and 4 weeks of normal chow (Figure I in the Data Supplement).[5,6]

CLIO-CyAm7 Studies of Rabbit Atherosclerosis and Triggered Atherothrombosis

Rabbits with atheroma underwent intravenous injection of NIRF USPIO nanoparticles (n=21, CLIO-CyAm7 group, Figure II in the Data Supplement) or saline (n=3) at the end of the preparation protocol. Rabbits were euthanized at 24 hours or underwent 2 rounds of thrombosis triggering 24 hours apart with Russell viper venom (0.15 mg/kg intraperitoneally; Sigma Chemical Co) followed 30 minutes later by histamine (0.02 mg/kg intravenously, Sigma Chemical Co). Rabbits underwent intravascular NIRF and ultrasound (IVUS) imaging during the double-triggering protocol (Figure I in the Data Supplement). A subgroup of rabbits (n=7) also underwent assessment for impaired endothelial permeability assessed by Evans Blue dye leakage (6 mL intravenous injection 0.5%; Sigma Chemical Co) 30 minutes before euthanization.[8] A higher dose of CLIO-CyAm7 (5.0 mg/kg) was used in these rabbits to overcome partial fluorescence overlap with Evans Blue.

In Vivo Intra-Arterial NIRF Molecular Imaging and IVUS Structural Imaging

Intravascular 2-Dimensional NIRF Molecular Imaging

Before pharmacological triggering, 15 rabbits underwent in vivo intravascular NIRF imaging of CLIO-CyAm7 deposition using a custom-built standalone 2-dimensional (2D) NIRF catheter-based system (750 nm laser excitation).[9] Four 90 to 100 mm pullbacks from the iliac bifurcation to the renal arteries were performed through blood, without flushing.[9,10] The peak target/background ratio was calculated for regions of atheroma across all pullbacks (MATLAB R2011a MathWorks). Regions with a luminal diameter of >5 mm were excluded because of NIR light attenuation.

IVUS Structural Assessment of Atherosclerosis and Atherothrombosis

IVUS images (Galaxy IVUS System, Boston Scientific) interrogated atheroma structure before triggering, and then after triggering to identify large luminal thrombi. IVUS images were coregistered to NIRF images using radiopaque markers on x-ray angiography. IVUS pre- and post-triggering images were coregistered to each other using side branches as fiducial markers.

Analysis of CLIO-CyAm7 Nanoparticle Distribution in Atheroma and Atherothrombosis

After euthanization, rabbits underwent fluorescence reflectance imaging, fluorescence microscopy, and histopathology analyses to determine the distribution of CLIO-CyAm7 nanoparticles in atheroma (NIH ImageJ). The percent positive CLIO-CyAm7 pixels were calculated in the superficial 100 μm of uniformly thresholded fluorescence microscopy images. In sections from rabbits injected with Evans Blue, the maximum distance from the luminal plaque surface to the deepest CLIO-CyAm7 signal, the Evans Blue signal, or internal elastic membrane (plaque thickness) were measured. Correlation coefficients were calculated to determine the relationship between these depths. See Data Supplement for details.

Statistical Analysis

For all analyses between 2 groups, nonparametric Mann–Whitney *U* test was used (GraphPad Prism v5.0, San Diego, CA). Thresholds for specificity and sensitivity calculations were determined using a receiver operator curve optimization. Data are presented as mean±SD or 95% confidence intervals.

Results

CLIO-CyAm7 Nanoparticles Localize to the Luminal Surface of Atheroma

Although USPIO nanoparticles are well-established cellular magnetic resonance imaging reporters for atherosclerosis,[11–13] their precise cellular and topographical distribution in coronary artery–sized atheroma is incompletely understood. NIRF nanoparticles allowed assessment of USPIO uptake in rabbit atheroma using fluorescence imaging (Figures 1 and 2). Ex vivo macroscopic and microscopic NIR fluorescence imaging illuminated plaque areas with high CLIO-CyAm7 uptake (Figure 1A). In contrast, minimal NIRF signal emerged in control rabbits receiving saline (Figure 1B), in accord with previous results.[9,14–16] Aortic atheroma exhibited increased CLIO-CyAm7 nanoparticle signal compared with control areas (Figure 1C, signal-to-noise ratio 18.1±11.3 versus 10.64±1.2 in the uninjured renal artery, P=0.03). On fluorescence microscopy, CLIO-CyAm7 primarily accumulated in the superficial intima, with a smaller component in deeper plaque regions (Figures 1D, 1E, and 2). CLIO-CyAm7 deposition was not uniform circumferentially across the atheroma surface (Figure 1D). Fluorescence microscopic analysis of the superficial intima demonstrated increased CLIO-CyAm7+ deposition in atheroma compared with the uninjured aorta (Figure 1F, 1.73±1.9% versus 0.13±0.28%, P<0.0001).

Cellular Distribution of Iron Oxide Nanoparticles in Atheroma

USPIO nanoparticles seem to localize primarily in macrophages in atheroma,[11,17,18] but detailed assessment of USPIO localization in other atheroma cells is limited. We, therefore, examined the cellular localization of CLIO-CyAm7 within plaque macrophages (Figure 2A2), smooth muscle cells (SMCs; Figure 2A3), and endothelial cells (Figure 2A1) and found evidence of CLIO-CyAm7 deposition within each of these 3 cell types (Figure 2). Analysis of representative sections from each triggered rabbit demonstrated restriction of

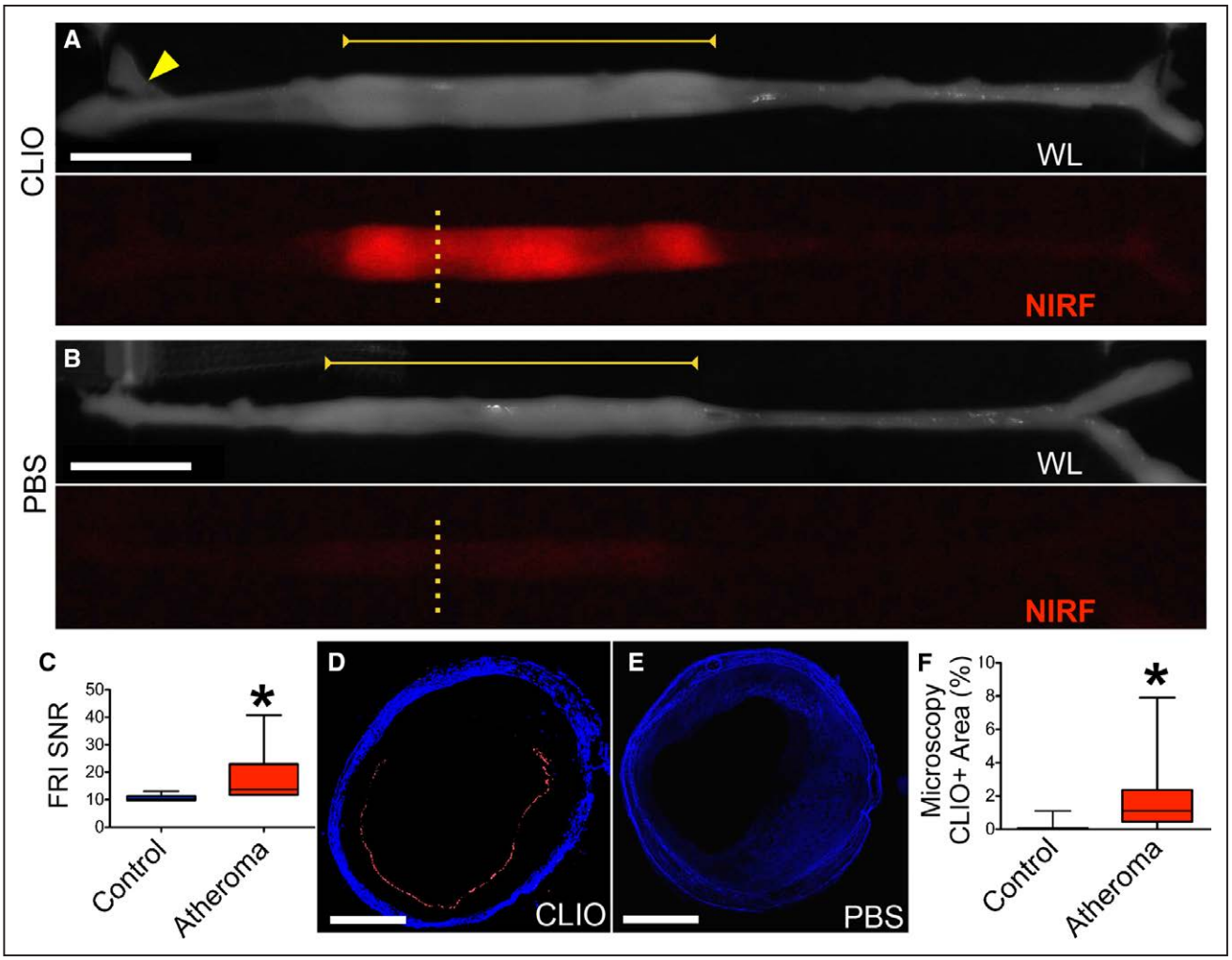

Figure 1. Ex vivo assessment of near-infrared fluorescence (NIRF) nanoparticle deposition in atheroma. **A**, Representative ex vivo fluorescence reflectance imaging (FRI) in a rabbit 24 h after cross-linked iron oxide (CLIO)-CyAm7 injection. White light image shows the resected aorta, stretched to premortem length determined by in vivo x-ray angiography. CLIO-CyAm7 signal evolved in atheroma (yellow bar) in contrast to minimal signal in the uninjured aorta, iliac bifurcation, or renal artery (yellow arrow). **B**, Ex vivo FRI of a rabbit injected with PBS as a control exhibits minimal NIRF signal in atheroma (horizontal yellow bar). **C**, Quantification of FRI signal in untriggered animals (n=6) showing significantly higher CLIO-CyAm7 signal in regions of atheroma compared with control renal artery (P=0.03). **D**, Corresponding fluorescence microscopy (FM, yellow dashed line in **A**) of CLIO-CyAm7–injected atheroma showing luminal surface CLIO-CyAm7 signal (red) noncircumferentially distributed. **E**, FM of a control atheroma (PBS injection, yellow dashed line in **B**) showing minimal CLIO-CyAm7 signal despite substantial atheroma detectable by autofluorescence. **F**, FM analysis of percent positive CLIO-CyAm7 pixels in experimental, triggered rabbits at 48 h showing increased CLIO-CyAm7 accumulation in regions of atheroma vs uninjured aorta without evidence of intimal thickening (P<0.0001, n=183 slices). Scale bars; FRI=1 cm, Microscopy=1 mm. CLIO-CyAm7=red, autofluorescence=blue.

the CLIO-CyAm7 signal to the luminal plaque surface in the majority of rabbits (67%), despite the presence of numerous cells deeper within the atheroma (Figure 2A). This observation suggested that restricted diffusion could also govern nanoparticle deposition.

The remaining 33% of rabbits showed evidence of deeper CLIO-CyAm7 deposition at the intimal-medial border (Figure 2B). CD31 staining for endothelial cells showed evidence of neovascularization in these deeper regions, providing a plausible access route for nanoparticles to deposit more deeply into atheroma. Although CLIO-CyAm7 localized near the CD31+ neovasculature (Figure 2B1), CLIO-CyAm7 signal did not localize to CD31+ cells, but rather targeted nearby macrophages identified by RAM11 staining (Figure 2B2).

CLIO-CyAm7 Deposits in Areas of Impaired Endothelial Permeability

Evidence of heterogeneous CLIO-CyAm7 distribution across the atheroma surface (Figure 1D) and within areas of neovascularization (Figure 2B) indicated that CLIO-CyAm7 deposition could relate to regional alterations in endothelial permeability. We, therefore, tested this hypothesis by coinjecting Evans Blue, a fluorescent azo dye that binds albumin. Evans blue deposition in the intima indicates increased, abnormal endothelial permeability.[16,19] After coinjection of Evans Blue in rabbits injected with CLIO-CyAm7, atheroma exhibited varying degrees of Evans Blue uptake (Figure 3). The depth of Evans Blue fluorescence signal in plaques correlated well with the depth of CLIO-CyAm7 penetration (r=0.64, P=0.003, Figure 3E). The depth of Evans blue penetration,

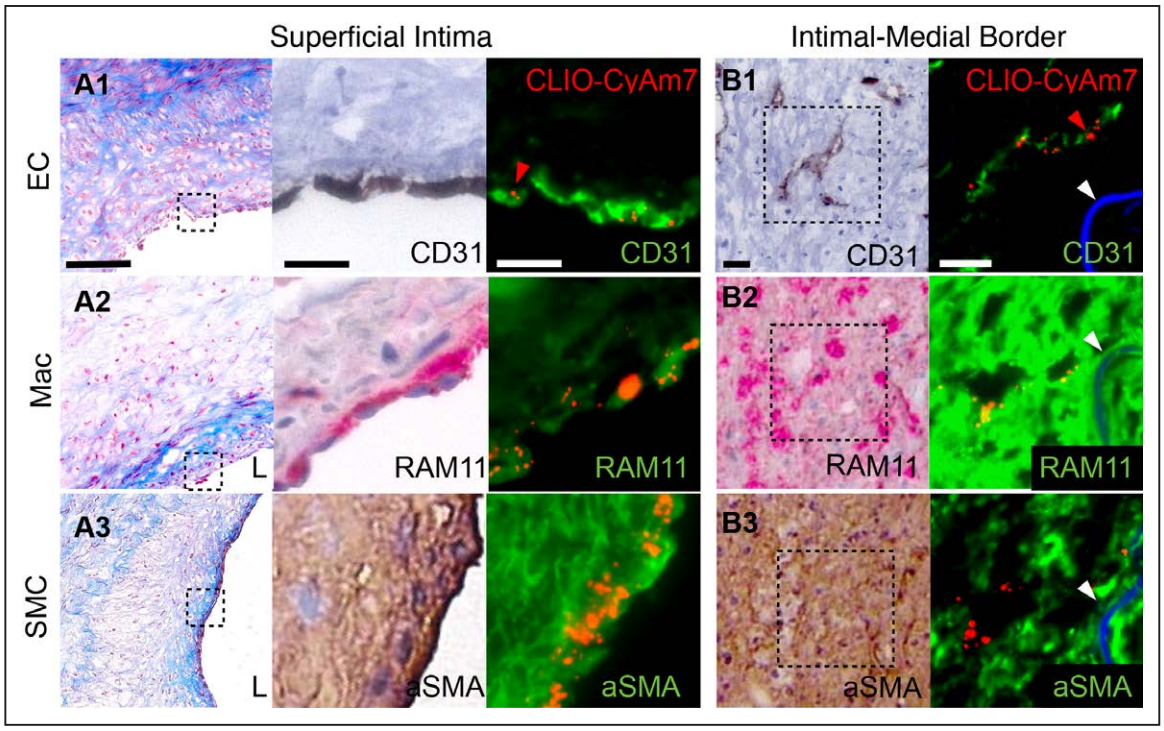

Figure 2. Cellular distribution of cross-linked iron oxide (CLIO)-CyAm7 nanoparticles in atherosclerosis. CLIO-CyAm7 uptake by plaque endothelial cells (ECs), macrophages, and smooth muscle cells (SMCs). Carstairs' stain shows the structural characteristics of atheroma, including collagen (blue). **A**, Carstairs', immunohistochemical, and immunofluorescence stains for CD31 (**A1**), RAM11 (**A2**), and α-smooth muscle actin (aSMA, **A3**) show correspondence between CLIO-CyAm7 signal (indicated by red arrows) and superficial, luminal ECs, macrophages, and SMCs, respectively. **B**, Distribution of CLIO-CyAm7 along the intimal-medial border in regions of neovasculature as detected by CD31 stain (**B1**). CLIO-CyAm7 deposition occurred in areas of RAM11+ macrophages flanking the neovasculature (**B2**). Immunohistochemical: RAM11+=red; CD31+ and aSMA+=brown. FM fusion images: CLIO-CyAm7=red, immunofluorescence antibodies=green, autofluorescence=blue. White arrows=internal elastic membrane. Scale bars, low magnification Carstairs'=100 μm, immunofluorescence and immunohistochemical=25 μm. L=vessel lumen.

however, did not relate to the overall plaque thickness (r=0.12, P=0.61, Figure 3D and 3F).

In Vivo NIRF Molecular Imaging of CLIO-CyAm7 Deposition

In vivo detection of CLIO-CyAm7 nanoparticle deposition in atheroma could offer an approach to detect biologically high-risk plaques. Further experiments, therefore, investigated whether CLIO-CyAm7 could provide sufficient signal to enable intravascular NIRF imaging of atheroma in vivo. Intravascular NIRF imaging is a high-resolution approach emerging for molecular imaging of coronary artery–sized vessels.[20–22] Multimodality imaging, including x-ray angiography, 2D NIRF, and IVUS imaging, was performed before triggering (Figure 4A through 4C, n=15 rabbits). Intravascular NIRF imaging performed through blood[9] demonstrated the ability to detect NIRF nanoparticle signal in areas of IVUS-confirmed atheroma (Figure 4B and 4C).

After pharmacological triggering with Russell viper venom and histamine to induce atherothrombosis, follow-up IVUS imaging at 48 hours revealed new luminal thrombi overlying areas of atheroma (Figure 4C and 4D). The average luminal diameter as measured by IVUS was 3.41±0.78 mm (range 1.93–5.87 mm), with some animals developing aneurysms (Figure 4G). Of note, multiple segments were larger than the typical 2.5 to 3.5 mm diameter of human coronary arteries to which the intravascular NIRF system is optimally calibrated.[9]

Ex vivo fluorescence reflectance imaging at 72 hours after initial CLIO-CyAm7 injection still detected CLIO-CyAm7 in atheroma (Figure 4F). Atheroma generated a significantly higher peak target/background ratio compared with the uninjured control aorta (peak target/background ratio 2.86±1.82 versus 1.55±0.65, P=0.001, respectively, Figure 4H; Figure III in the Data Supplement).

CLIO-CyAm7 Nanoparticle Deposition Underlies Areas of Plaque Thrombosis In Vivo and by Histological Analysis

Ten of 15 rabbits (67%) undergoing pharmacological triggering developed plaque thrombosis as confirmed by histological examination (Figure 5). A total of 21 of 51 atheroma segments compiled from all rabbits exhibited adherent thrombus (41%) on Carstairs' staining. In vivo IVUS images demonstrated thrombus in 4 of 9 rabbits with confirmation on Carstairs' stain after euthanization. IVUS-detectable thrombi were larger than those identified by Carstairs' alone (4.4±5.0 μm^2 versus 0.42±0.39 μm^2), suggesting that IVUS had lower sensitivity to detect smaller thrombi.

Quantitative analysis revealed that the 21 plaques with adherent Carstairs'-positive thrombus exhibited higher CLIO-CyAm7 accumulation than the 30 plaques without thrombus (Figure 5C, 2.1±1.7% versus 1.5±1.9%, respectively, P=0.045). CLIO-CyAm7 nanoparticles abutted thrombi, particularly at plaque shoulders (Figure 5D and 5G). Receiver

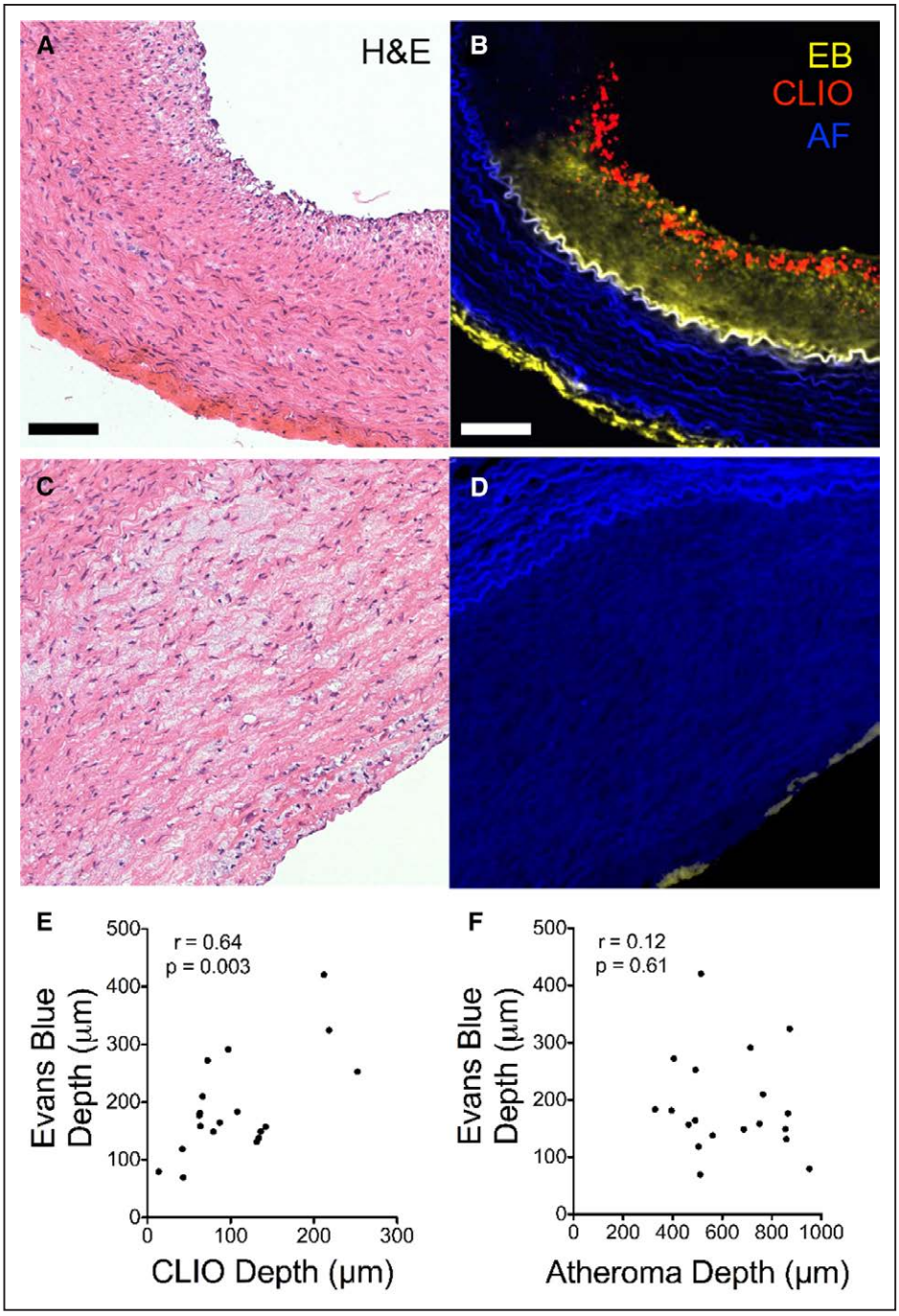

Figure 3. Plaque endothelial permeability assessed with Evans Blue concomitantly with cross-linked iron oxide (CLIO)-CyAm7 nanoparticle deposition. A subgroup of rabbits injected with CLIO-CyAm7 also received Evans Blue shortly before euthanization. **A**, Atheroma with extensive Evans blue uptake (yellow) throughout the intima limited peripherally by the internal elastic membrane (autofluorescence, AF, blue). CLIO-CyAm7 (red) similarly penetrates below the endothelial layer throughout the intima. **B**, Atheroma with minimal, superficial Evans blue uptake and minimal CLIO-CyAm7 signal. **C**, Evans Blue and CLIO-CyAm7 depths of penetration correlated strongly (r=0.64, P=0.003, n=19). **D**, Weak correlation between the depth of Evans Blue penetration and plaque thickness (r=0.14, P=0.61, n=19). Scale bar, 100 μm. H&E indicates hematoxylin and eosin.

operator curve analysis determined that the optimal threshold for CLIO-CyAm7 positivity on fluorescence microscopy was 0.85% positive area (Figure IV in the Data Supplement). This threshold provided a sensitivity and specificity of 82.6% (confidence intervals, 61.2%–95%) and 61.8% (confidence intervals, 43.6%–77.8%), respectively, for plaque thrombosis. Using this threshold criterion, the positive predictive value of a CLIO-positive plaque for plaque thrombosis was 59.4% (confidence intervals, 40.6%–76.3%) and the negative predictive value was 84.0% (confidence intervals, 63.9%–95.4%).

Discussion

Atherosclerosis progression and plaque destabilization involves the interplay between multiple cell types, including

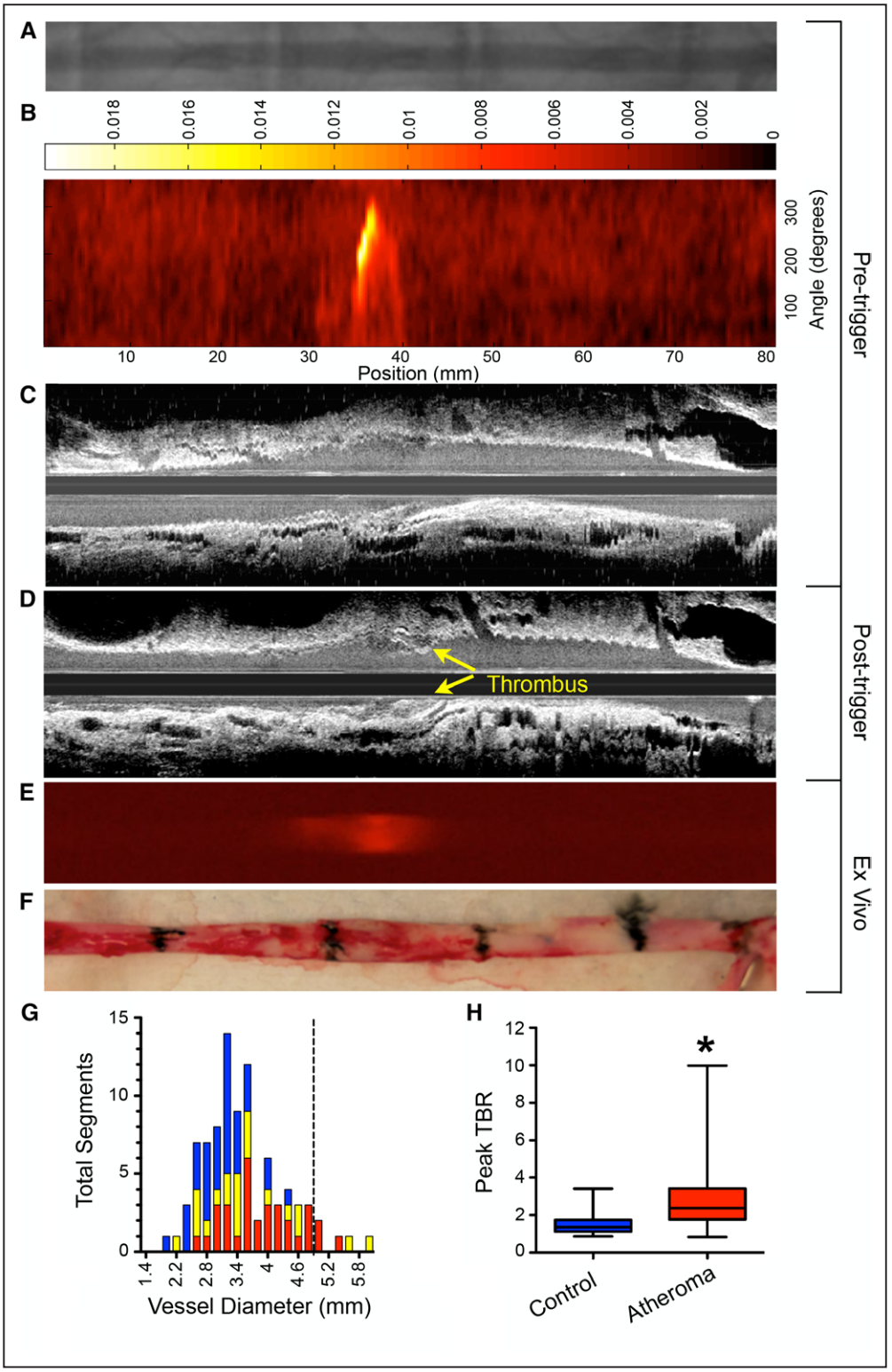

Figure 4. In vivo and ex vivo near-infrared fluorescence (NIRF) imaging of atherothrombosis. Rabbits underwent the protocol described in Figure I in the Data Supplement. **A**, Pre-trigger x-ray angiography showing the aorta for image coregistration (not shown are the iliac bifurcation and renal artery). **B**, Pre-trigger in vivo NIRF imaging projected into a 2-dimensional (2D) matrix of translational distance (*x*-axis) and 0 to 360 degree of rotation (*y*-axis). **C** and **D**, Pre- and post-trigger intravascular ultrasound (IVUS) imaging showing triggered luminal thrombus (yellow arrows) corresponding to the region of increased NIRF signal intensity on pretrigger NIRF imaging in **B**. **E**, Ex vivo fluorescence reflectance imaging of cross-linked iron oxide (CLIO)-CyAm7 corroborating in vivo 2D NIRF imaging. **F**, Gross pathology of the resected aorta with 1.5 cm black tissue markings for histological analysis and coregistration with in vivo imaging above. **G**, Histogram of vessel diameter measured by cross-sectional IVUS imaging. Red indicates atheroma without attached thrombus, yellow indicates atheroma with attached thrombus, and blue indicates uninjured control aortic segments. The dashed line indicates the 5 mm cutoff for exclusion of NIRF imaging data because of distance attenuation of the NIRF signal in large vessels. **H**, In vivo 2D NIRF imaging showed significantly higher target/background ratio (TBR) in areas with atheroma, compared with uninjured segments of the aorta (peak TBR 2.86±1.82 and 1.55±0.65, P=0.001).

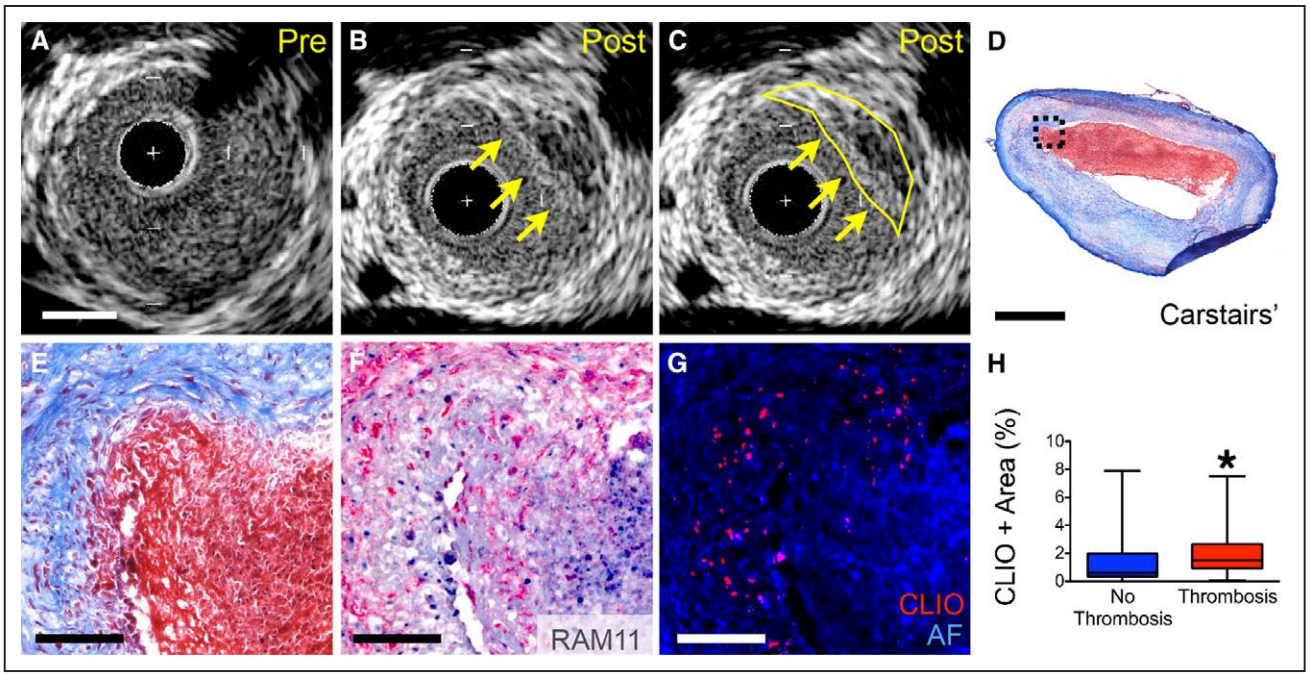

Figure 5. In vivo and microscopic analyses of nanoparticle deposition and triggered plaque thrombosis. **A**, Cross-sectional intravascular ultrasound (IVUS) image of rabbit aorta with atheroma before pharmacological triggering. **B** and **C**, Post-triggering IVUS image corresponding to (**A**) demonstrating new luminal irregularity (yellow arrows and outline) consistent with new thrombus (segmented in **C**). **D** and **E**, Corresponding histology of plaque with adherent thrombus. Carstairs' staining of fibrin rich adherent thrombus (red). **F**, RAM11+ macrophages are present at the surface below the thrombus. **G**, Epifluorescence microscopy revealing increased cross-linked iron oxide (CLIO)-CyAm7 (red) at the plaque shoulder and underlying areas of thrombus. **H**, Significantly higher CLIO-CyAm7 accumulation occurred in regions with thrombosis compared with atheroma without thrombosis (2.1±1.7%, n=34, and 1.5±1.9%, n=23, respectively, *P*=0.045). Scale bars, IVUS and low magnification histology=1 mm, high-magnification histology=100 μm.

macrophages, endothelial cells, and SMCs. This study investigated the role of impaired endothelial permeability and atheroma cell distribution by assessing the distribution of NIRF CLIO-CyAm7 nanoparticles[12,17] in experimental atherothrombosis. The overall results demonstrate that plaques that exhibit impaired endothelial permeability and surface atheroma cellularity have heightened susceptibility to subsequent thrombosis. From an imaging standpoint, the current data sharpen the understanding of nanoparticle targeting in atheroma. USPIO nanoparticles can deposit in all major atheroma cell types and specifically in areas of impaired endothelial permeability, as supported by Evans Blue deposition and neovessel presence. In addition, CLIO-CyAm7 enables intravascular NIRF imaging of various atheroma cell types and altered endothelial permeability in vivo through blood, offering the potential for translational detection of biologically high-risk plaques.

Despite evaluation of USPIO in several experimental and clinical atherosclerosis studies, the precise targeting profile of USPIO nanoparticles in atherosclerosis is incompletely understood. The current investigation leveraged the engineered fluorescence capabilities of the CLIO-CyAm7 USPIO nanoparticle and examined over 50 plaques in the rabbit aorta, a vessel of similar caliber as human coronary arteries. Although USPIOs are established macrophage reporter agents, nonmacrophage cells might also contribute to USPIO retention in atherosclerosis.[19,23–25] This study confirmed that USPIOs could not only target plaque macrophages but also target some periluminal plaque SMCs and intimal endothelial cells. SMCs undergo phenotypic changes in the inflammatory milieu of the atherosclerotic plaque.[26–28] Lesional SMCs bear adhesion molecules, class II major histocompatibility molecules, and tissue factor, indicating inflammatory activation and the potential to drive atherothrombosis.[26,28–33] Inflammatory SMCs can, thus, phagocytose CLIO-CyAm7 given its similar size compared with low density lipoprotein.[25,34] In this regard, the nanoparticle preparation ferumoxtran, a clinical analog of CLIO, can localize within cells with both SMC- and macrophage-like characteristics on electron microscopy.[17,24] The overall findings extend previous work by showing that USPIO nanoparticles accumulate in macrophages, pathological endothelial cells, and inflammatory SMCs.[19,24,34–36]

This study demonstrated that USPIO nanoparticle deposition was heterogeneous, even across a plaque's circumference (Figure 1D). Histological analyses revealed that CLIO-CyAm7 deposited primarily within the first 100 μm of the plaque surface, despite abundant plaque cells, including macrophages, throughout deeper regions of the plaques. The heterogeneous distribution of CLIO nanoparticles in atheroma suggested that altered endothelial permeability in atherosclerosis could modulate nanoparticle deposition, a phenomenon identified in cancer studies as the enhanced permeability and retention effect.[37] This hypothesis was confirmed when Evans blue deposition identified impaired endothelial permeability consistently in areas of CLIO-CyAm7 deposition. The depth of Evans Blue stain further correlated with the depth of CLIO-CyAm7 penetration, indicating that enhanced plaque permeability tracked with impaired endothelial permeability (Figure 3).

These results provide evidence that impaired endothelial barrier function, often but variably present in atherosclerosis, links to USPIO deposition in atheroma. These findings parallel those in arteriovenous fistulae that also exhibit pathological endothelial permeability[19] and is further supported by CLIO-CyAm7 accumulation in deeper plaque macrophages adjacent to areas of microvascular CD31+ endothelial cells (Figure 2B). Neovascularization, the growth of the vasa vasorum from the adventitia to the media and eventually in the deep intima, promotes intraplaque hemorrhage due to the fragile, leaky neovessels, and increases the risk of plaque rupture.[38] Thus, USPIO nanoparticle localization in the atheroma intima and regions of neovascularization illuminates impaired endothelial barrier function in atherosclerosis. This capability might also have future application to assess superficial plaque erosion, a mechanism of coronary thrombosis of increasing interest in the current era.[3]

Attesting to the important pathological consequences of impaired endothelial barrier function and atheroma proinflammatory cells, plaques that developed triggered thrombosis showed enhanced USPIO nanoparticle uptake (Figure 5H). Nanoparticle deposition further occurred at plaque shoulders, areas associated with plaque disruption, and subsequent thrombosis. These findings suggest that USPIO nanoparticles distinguish specific atheroma and even regions of atheroma prone to develop thrombosis, and imaging of USPIO deposition might prove useful in enhancing subject-specific and plaque-specific risk of atherothrombotic events.

Alternative approaches to detect impaired endothelial permeability include dynamic contrast–enhanced magnetic resonance imaging using albumin-binding contrast agents[6,8,39,40] or indocyanine green–based NIRF imaging.[15,16] Comparatively, CLIO-CyAm7 may provide more durable cellular uptake, including into macrophages, endothelial cells, and SMCs, and therefore can also serve as a reporter of cellular inflammation. Compared with magnetic resonance imaging approaches, which have enabled clinical molecular magnetic resonance imaging of inflamed carotid plaques,[12,17] higher resolution imaging approaches appear necessary for coronary artery imaging.[20–22] In a translational substudy, we leveraged the NIRF capabilities of the CLIO-CyAm7 USPIO to perform intravascular NIRF imaging, a clinically emerging approach for high-resolution imaging of human coronary arteries.[20–22,41–43] In vivo NIRF imaging of CLIO-CyAm7 deposition in coronary-sized vessels demonstrated significantly higher NIRF signal in rabbit aortic plaques than in control areas. The results demonstrate a new capability of NIRF imaging to assess atheroma cellularity and because of impaired endothelial barrier function in vivo. The current intravascular NIRF imaging results have promising clinical applicability, as NIR fluorophores,[15,44] USPIOs,[12,17] and intracoronary NIRF imaging[42] are clinically translatable.

This study has certain limitations. Although triggering often provoked the formation of adherent thrombi, these sites rarely displayed plaque rupture characterized by a disrupted fibrous cap, a potential difference with human atherothrombosis, although plaque rupture has been previously described after this pharmacological triggering procedure.[45–47] However, this finding of mural thrombosis at sites of defective endothelial barrier function enhances the relevance of the present findings to superficial erosion, an increasingly recognized cause of acute coronary syndrome. These results further agree with the findings on thrombosed lesions observed in myocardial infarction–prone atherosclerotic rabbits treated with a spasmogenic triggering regimen.[48] Higher-resolution confocal microscopic colocalization of CLIO-CyAm7 nanoparticles with cell-specific fluorescence antibodies was not possible, as commercial confocal systems are not equipped with 750 nm range lasers; we therefore used epifluorescence colocalization approaches. Finally, in vivo fluorescence reflectance imaging is limited in a distance-dependent manner as described previously, resulting in semiquantitative NIRF signal assessment.[9] NIRF imaging has limited depth sensing, and therefore atheroma within aneurysmal segments (eg, 5.0 mm diameter, larger than a typical coronary artery) did not produce detectable in vivo NIRF signal. Since completion of this study, a combined optical coherence tomography–NIRF catheter became available for integrated molecular-structural imaging[49]; however, optical coherence tomography signal detection requires saline-flushing, unlike the current standalone NIRF approach performed through flowing blood, without flushing.

In conclusion, this study demonstrates that USPIO nanoparticles deposit in plaque macrophages, SMCs and endothelial cells associated with zones of impaired surface endothelial permeability as well as zones of neovascularization. Nanoparticle deposition further occurs in plaques that progress to thrombosis. These results shed new mechanistic light into the pathophysiology of the thrombotic complications of atherosclerosis. Furthermore, intravascular imaging of NIRF nanoparticles may provide a novel translational approach to detect biologically high-risk plaques in vivo.

Acknowledgments

We thank Dr George Mallas for assistance with intravascular 2-dimensional near-infrared fluorescence imaging and Dr Lang Wang for performing additional control experiments.

Sources of Funding

This study was supported by National Institutes of Health R01HL108229 and R01HL122388 (Dr Jaffer) and HL080472 (Dr Libby), American Heart Association grants no. 12PRE11160000 (Dr Stein-Merlob); no. 13POST14640021 (Dr Hara); no. 13GRNT17060040 (Dr Jaffer), Deutsche Forschungsgemeinschaft as part of the CRC 1123 (Z1) (Dr Ntziachristos), the Kanae Foundation for Research Abroad (Dr Hara), and the MGH Hassenfeld Clinical Scholar Award (Dr Jaffer).

Disclosures

Dr Libby has had sponsored research grants from General Electric, GlaxoSmithKline, and Novartis. Dr Jaffer has sponsored research grants from Kowa, Siemens, and Canon, has a consulting agreement with Boston Scientific and Abbott Vascular. Massachusetts General Hospital has a patent licensing arrangement with Canon Corporation, and Dr Jaffer has the right to receive licensing royalties.

References

1. Libby P. Mechanisms of acute coronary syndromes and their implications for therapy. *N Engl J Med*. 2013;368:2004–2013. doi: 10.1056/NEJMra1216063.
2. Virmani R, Burke AP, Farb A, Kolodgie FD. Pathology of the vulnerable plaque. *J Am Coll Cardiol*. 2006;47(suppl 8):C13–C18. doi: 10.1016/j.jacc.2005.10.065.
3. Libby P, Pasterkamp G. Requiem for the 'vulnerable plaque'. *Eur Heart J*. 2015;36:2984–2987. doi: 10.1093/eurheartj/ehv349.

4. Gimbrone MA Jr, García-Cardeña G. Endothelial cell dysfunction and the pathobiology of atherosclerosis. *Circ Res*. 2016;118:620–636. doi: 10.1161/CIRCRESAHA.115.306301.
5. Phinikaridou A, Hallock KJ, Qiao Y, Hamilton JA. A robust rabbit model of human atherosclerosis and atherothrombosis. *J Lipid Res*. 2009;50:787–797. doi: 10.1194/jlr.M800460-JLR200.
6. Phinikaridou A, Ruberg FL, Hallock KJ, Qiao Y, Hua N, Viereck J, Hamilton JA. *In vivo* detection of vulnerable atherosclerotic plaque by MRI in a rabbit model. *Circ Cardiovasc Imaging*. 2010;3:323–332. doi: 10.1161/CIRCIMAGING.109.918524.
7. Abela OG, Ahsan CH, Alreefi F, Salehi N, Baig I, Janoudi A, Abela GS. Plaque rupture and thrombosis: the value of the atherosclerotic rabbit model in defining the mechanism. *Curr Atheroscler Rep*. 2016;18:29. doi: 10.1007/s11883-016-0587-0.
8. Phinikaridou A, Andia ME, Protti A, Indermuehle A, Shah A, Smith A, Warley A, Botnar RM. Noninvasive magnetic resonance imaging evaluation of endothelial permeability in murine atherosclerosis using an albumin-binding contrast agent. *Circulation*. 2012;126:707–719. doi: 10.1161/CIRCULATIONAHA.112.092098.
9. Jaffer FA, Calfon MA, Rosenthal A, Mallas G, Razansky RN, Mauskapf A, Weissleder R, Libby P, Ntziachristos V. Two-dimensional intravascular near-infrared fluorescence molecular imaging of inflammation in atherosclerosis and stent-induced vascular injury. *J Am Coll Cardiol*. 2011;57:2516–2526. doi: 10.1016/j.jacc.2011.02.036.
10. Osborn EA, Jaffer FA. The year in molecular imaging. *JACC Cardiovasc Imaging*. 2010;3:1181–1195. doi: 10.1016/j.jcmg.2010.09.009.
11. Morishige K, Kacher DF, Libby P, Josephson L, Ganz P, Weissleder R, Aikawa M. High-resolution magnetic resonance imaging enhanced with superparamagnetic nanoparticles measures macrophage burden in atherosclerosis. *Circulation*. 2010;122:1707–1715. doi: 10.1161/CIRCULATIONAHA.109.891804.
12. Tang TY, Howarth SP, Miller SR, Graves MJ, Patterson AJ, U-King-Im JM, Li ZY, Walsh SR, Brown AP, Kirkpatrick PJ, Warburton EA, Hayes PD, Varty K, Boyle JR, Gaunt ME, Zalewski A, Gillard JH. The ATHEROMA (Atorvastatin Therapy: Effects on Reduction of Macrophage Activity) Study. Evaluation using ultrasmall superparamagnetic iron oxide-enhanced magnetic resonance imaging in carotid disease. *J Am Coll Cardiol*. 2009;53:2039–2050. doi: 10.1016/j.jacc.2009.03.018.
13. Tang TY, Muller KH, Graves MJ, Li ZY, Walsh SR, Young V, Sadat U, Howarth SP, Gillard JH. Iron oxide particles for atheroma imaging. *Arterioscler Thromb Vasc Biol*. 2009;29:1001–1008. doi: 10.1161/ATVBAHA.108.165514.
14. Jaffer FA, Vinegoni C, John MC, Aikawa E, Gold HK, Finn AV, Ntziachristos V, Libby P, Weissleder R. Real-time catheter molecular sensing of inflammation in proteolytically active atherosclerosis. *Circulation*. 2008;118:1802–1809. doi: 10.1161/CIRCULATIONAHA.108.785881.
15. Verjans JW, Osborn EA, Ughi GJ, Calfon Press MA, Hamidi E, Antoniadis AP, Papafaklis MI, Conrad MF, Libby P, Stone PH, Cambria RP, Tearney GJ, Jaffer FA. Targeted near-infrared fluorescence imaging of atherosclerosis: clinical and intracoronary evaluation of indocyanine green. *JACC Cardiovasc Imaging*. 2016;9:1087–1095. doi: 10.1016/j.jcmg.2016.01.034.
16. Vinegoni C, Botnaru I, Aikawa E, Calfon MA, Iwamoto Y, Folco EJ, Ntziachristos V, Weissleder R, Libby P, Jaffer FA. Indocyanine green enables near-infrared fluorescence imaging of lipid-rich, inflamed atherosclerotic plaques. *Sci Transl Med*. 2011;3:84ra45. doi: 10.1126/scitranslmed.3001577.
17. Kooi ME, Cappendijk VC, Cleutjens KB, Kessels AG, Kitslaar PJ, Borgers M, Frederik PM, Daemen MJ, van Engelshoven JM. Accumulation of ultrasmall superparamagnetic particles of iron oxide in human atherosclerotic plaques can be detected by *in vivo* magnetic resonance imaging. *Circulation*. 2003;107:2453–2458. doi: 10.1161/01.CIR.0000068315.98705.CC.
18. Trivedi RA, U-King-Im JM, Graves MJ, Kirkpatrick PJ, Gillard JH. Noninvasive imaging of carotid plaque inflammation. *Neurology*. 2004;63:187–188.
19. Cui J, Kessinger CW, McCarthy JR, Sosnovik DE, Libby P, Thadhani RI, Jaffer FA. *In vivo* nanoparticle assessment of pathological endothelium predicts the development of inflow stenosis in murine arteriovenous fistula. *Arterioscler Thromb Vasc Biol*. 2015;35:189–196. doi: 10.1161/ATVBAHA.114.304483.
20. Jaffer FA, Verjans JW. Molecular imaging of atherosclerosis: clinical state-of-the-art. *Heart*. 2014;100:1469–1477. doi: 10.1136/heartjnl-2011-301370.
21. Mulder WJ, Jaffer FA, Fayad ZA, Nahrendorf M. Imaging and nanomedicine in inflammatory atherosclerosis. *Sci Transl Med*. 2014;6:239sr1. doi: 10.1126/scitranslmed.3005101.
22. Bourantas CV, Jaffer FA, Gijsen FJ, van Soest G, Madden SP, Courtney BK, Fard AM, Tenekecioglu E, Zeng Y, van der Steen AF, Emelianov S, Muller J, Stone PH, Marcu L, Tearney GJ, Serruys PW. Hybrid intravascular imaging: recent advances, technical considerations, and current applications in the study of plaque pathophysiology. *Eur Heart J*. 2016;38:400–412.
23. Jaffer FA, Nahrendorf M, Sosnovik D, Kelly KA, Aikawa E, Weissleder R. Cellular imaging of inflammation in atherosclerosis using magnetofluorescent nanomaterials. *Mol Imaging*. 2006;5:85–92.
24. Ruehm SG, Corot C, Vogt P, Kolb S, Debatin JF. Magnetic resonance imaging of atherosclerotic plaque with ultrasmall superparamagnetic particles of iron oxide in hyperlipidemic rabbits. *Circulation*. 2001;103:415–422.
25. Hyafil F, Laissy JP, Mazighi M, Tchétché D, Louedec L, Adle-Biassette H, Chillon S, Henin D, Jacob MP, Letourneur D, Feldman LJ. Ferumoxtran-10-enhanced MRI of the hypercholesterolemic rabbit aorta: relationship between signal loss and macrophage infiltration. *Arterioscler Thromb Vasc Biol*. 2006;26:176–181. doi: 10.1161/01.ATV.0000194098.82677.57.
26. Doran AC, Meller N, McNamara CA. Role of smooth muscle cells in the initiation and early progression of atherosclerosis. *Arterioscler Thromb Vasc Biol*. 2008;28:812–819. doi: 10.1161/ATVBAHA.107.159327.
27. Lim S, Lee SY, Seo HH, Ham O, Lee C, Park JH, Lee J, Seung M, Yun I, Han SM, Lee S, Choi E, Hwang KC. Regulation of mitochondrial morphology by positive feedback interaction between PKCδ and Drp1 in vascular smooth muscle cell. *J Cell Biochem*. 2015;116:648–660. doi: 10.1002/jcb.25016.
28. Wall VZ, Bornfeldt KE. Arterial smooth muscle. *Arterioscler Thromb Vasc Biol*. 2014;34:2175–2179. doi: 10.1161/ATVBAHA.114.304441.
29. Lim S, Park S. Role of vascular smooth muscle cell in the inflammation of atherosclerosis. *BMB Rep*. 2014;47:1–7.
30. Hansson GK, Jonasson L, Holm J, Claesson-Welsh L. Class II MHC antigen expression in the atherosclerotic plaque: smooth muscle cells express HLA-DR, HLA-DQ and the invariant gamma chain. *Clin Exp Immunol*. 1986;64:261–268.
31. Wilcox JN, Smith KM, Schwartz SM, Gordon D. Localization of tissue factor in the normal vessel wall and in the atherosclerotic plaque. *Proceed Natl Acad Sci USA*. 1989;86:2839–43.
32. Drake TA, Morrissey JH, Edgington TS. Selective cellular expression of tissue factor in human tissues. Implications for disorders of hemostasis and thrombosis. *Am J Pathol*. 1989;134:1087–1097.
33. Schönbeck U, Mach F, Sukhova GK, Herman M, Graber P, Kehry MR, Libby P. CD40 ligation induces tissue factor expression in human vascular smooth muscle cells. *Am J Pathol*. 2000;156:7–14. doi: 10.1016/S0002-9440(10)64699-8.
34. Yancy AD, Olzinski AR, Hu TC, Lenhard SC, Aravindhan K, Gruver SM, Jacobs PM, Willette RN, Jucker BM. Differential uptake of ferumoxtran-10 and ferumoxytol, ultrasmall superparamagnetic iron oxide contrast agents in rabbit: critical determinants of atherosclerotic plaque labeling. *J Magn Reson Imaging*. 2005;21:432–442. doi: 10.1002/jmri.20283.
35. Litovsky S, Madjid M, Zarrabi A, Casscells SW, Willerson JT, Naghavi M. Superparamagnetic iron oxide-based method for quantifying recruitment of monocytes to mouse atherosclerotic lesions in vivo: enhancement by tissue necrosis factor-alpha, interleukin-1beta, and interferon-gamma. *Circulation*. 2003;107:1545–1549.
36. Schmitz SA, Coupland SE, Gust R, Winterhalter S, Wagner S, Kresse M, Semmler W, Wolf KJ. Superparamagnetic iron oxide-enhanced MRI of atherosclerotic plaques in Watanabe hereditable hyperlipidemic rabbits. *Invest Radiol*. 2000;35:460–471.
37. Kobayashi H, Watanabe R, Choyke PL. Improving conventional enhanced permeability and retention (EPR) effects; what is the appropriate target? *Theranostics*. 2013;4:81–89. doi: 10.7150/thno.7193.
38. Sadat U, Jaffer FA, van Zandvoort MA, Nicholls SJ, Ribatti D, Gillard JH. Inflammation and neovascularization intertwined in atherosclerosis: imaging of structural and molecular imaging targets. *Circulation*. 2014;130:786–794. doi: 10.1161/CIRCULATIONAHA.114.010369.
39. Ibrahim T, Makowski MR, Jankauskas A, Maintz D, Karch M, Schachoff S, Manning WJ, Schömig A, Schwaiger M, Botnar RM. Serial contrast-enhanced cardiac magnetic resonance imaging demonstrates regression of hyperenhancement within the coronary artery wall in patients after acute myocardial infarction. *JACC Cardiovasc Imaging*. 2009;2:580–588. doi: 10.1016/j.jcmg.2008.12.029.
40. Kerwin WS, O'Brien KD, Ferguson MS, Polissar N, Hatsukami TS, Yuan C. Inflammation in carotid atherosclerotic plaque: a dynamic

contrast-enhanced MR imaging study. *Radiology*. 2006;241:459–468. doi: 10.1148/radiol.2412051336.
41. Osborn EA, Jaffer FA. The advancing clinical impact of molecular imaging in CVD. *JACC Cardiovasc Imaging*. 2013;6:1327–1341. doi: 10.1016/j.jcmg.2013.09.014.
42. Ughi GJ, Wang H, Gerbaud E, Gardecki JA, Fard AM, Hamidi E, Vacas-Jacques P, Rosenberg M, Jaffer FA, Tearney GJ. Clinical characterization of coronary atherosclerosis with dual-modality OCT and near-infrared autofluorescence imaging. *JACC Cardiovasc Imaging*. 2016;9:1304–1314.
43. Hara T, Ughi GJ, McCarthy JR, Erdem SS, Mauskapf A, Lyon SC, Fard AM, Edelman ER, Tearney GJ, Jaffer FA. Intravascular fibrin molecular imaging improves the detection of unhealed stents assessed by optical coherence tomography in vivo. *Eur Heart J*. 2017;38:447–455.
44. Whitley MJ, Cardona DM, Lazarides AL, Spasojevic I, Ferrer JM, Cahill J, Lee CL, Snuderl M, Blazer DG 3rd, Hwang ES, Greenup RA, Mosca PJ, Mito JK, Cuneo KC, Larrier NA, O'Reilly EK, Riedel RF, Eward WC, Strasfeld DB, Fukumura D, Jain RK, Lee WD, Griffith LG, Bawendi MG, Kirsch DG, Brigman BE. A mouse-human phase 1 co-clinical trial of a protease-activated fluorescent probe for imaging cancer. *Sci Transl Med*. 2016;8:320ra4. doi: 10.1126/scitranslmed.aad0293.
45. Phinikaridou A, Qiao Y, Giordano N, Hamilton JA. Detection of thrombus size and protein content by ex vivo magnetization transfer and diffusion weighted MRI. *J Cardiovasc Magn Reson*. 2012;14:45. doi: 10.1186/1532-429X-14-45.
46. Yamashita A, Asada Y. A rabbit model of thrombosis on atherosclerotic lesions. *J Biomed Biotechnol*. 2011;2011:424929. doi: 10.1155/2011/424929.
47. Yamashita A, Zhao Y, Zhao S, Matsuura Y, Sugita C, Iwakiri T, Okuyama N, Ohe K, Koshimoto C, Kawai K, Tamaki N, Kuge Y, Asada Y. Arterial (18)F-fluorodeoxyglucose uptake reflects balloon catheter-induced thrombus formation and tissue factor expression via nuclear factor-κB in rabbit atherosclerotic lesions. *Circ J*. 2013;77:2626–2635.
48. Shiomi M, Ishida T, Kobayashi T, Nitta N, Sonoda A, Yamada S, Koike T, Kuniyoshi N, Murata K, Hirata K, Ito T, Libby P. Vasospasm of atherosclerotic coronary arteries precipitates acute ischemic myocardial damage in myocardial infarction-prone strain of the Watanabe heritable hyperlipidemic rabbits. *Arterioscler Thromb Vasc Biol*. 2013;33:2518–2523. doi: 10.1161/ATVBAHA.113.301303.
49. Yoo H, Kim JW, Shishkov M, Namati E, Morse T, Shubochkin R, McCarthy JR, Ntziachristos V, Bouma BE, Jaffer FA, Tearney GJ. Intra-arterial catheter for simultaneous microstructural and molecular imaging in vivo. *Nat Med*. 2011;17:1680–1684. doi: 10.1038/nm.2555.

CLINICAL PERSPECTIVE

The majority of acute coronary syndrome result from focal thrombosis arising from atherosclerosis. The mechanisms underlying plaque thrombosis have evolved from a unique focus on the disruption of a thin fibrous cap to also incorporate superficial plaque erosion, an entity more prevalent in smokers and younger women. These 2 causes of atherothrombosis share a common pathobiology involving diseased endothelial cells, and therefore an approach to understand impaired endothelial function in vivo could provide new mechanistic and predictive insights into atherothrombosis. In this experimental atherothrombosis study, we investigated in vivo mechanisms of impaired endothelial function using the engineered near-infrared fluorescence nanoparticle cross-linked iron oxide-CyAm7. After intravenous injection of nanoparticles into atheroma-bearing rabbits, near-infrared fluorescence microscopy demonstrated that cross-linked iron oxide-CyAm7 nanoparticles localized in the superficial intima as well as regions of plaque neovascularization, and further accumulated in multiple atheroma cell types, including macrophages, endothelial cells, and smooth muscle cells. Co-injection of Evans Blue dye moreover revealed that cross-linked iron oxide-CyAm7 deposited in areas of impaired endothelial barrier function. In rabbits subjected to a modified Constantinides' model of triggered atherothrombosis, thrombosed plaques exhibited significantly higher cross-linked iron oxide-CyAm7 accumulation than nonthrombosed plaques. Finally, intravascular near-infrared fluorescence imaging, a high-resolution translatable molecular imaging approach for coronary artery disease, detected nanoparticles in atheroma in vivo ($P<0.05$ versus reference segments). The overall results provide new evidence that iron oxide nanoparticles report on plaque cells resident in areas of impaired endothelial barrier function, and that intravascular near-infrared fluorescence molecular imaging may provide a translatable approach to mechanistically investigate and predict atherothrombosis.

Circulation
Cardiovascular Imaging

Atheroma Susceptible to Thrombosis Exhibit Impaired Endothelial Permeability In Vivo as Assessed by Nanoparticle-Based Fluorescence Molecular Imaging

Ashley F. Stein-Merlob, Tetsuya Hara, Jason R. McCarthy, Adam Mauskapf, James A. Hamilton, Vasilis Ntziachristos, Peter Libby and Farouc A. Jaffer

Circ Cardiovasc Imaging. 2017;10:
doi: 10.1161/CIRCIMAGING.116.005813
Circulation: Cardiovascular Imaging is published by the American Heart Association, 7272 Greenville Avenue, Dallas, TX 75231

Print ISSN: 1941-9651. Online ISSN: 1942-0080

Supplemental Material

METHODS

Animal Model of Atherothrombosis

New Zealand white rabbits (n=31, weight 3-4kg, Charles River Laboratories) at 3-4 months of age consumed a 1% high cholesterol diet (HCD, Research Diets, Inc., New Brunswick, NJ) for 2 weeks prior to aortic balloon injury of the abdominal aorta followed by another six weeks of 1% HCD and four weeks of normal chow diet (Supplemental Figure 1).[1, 2] Balloon injury using a 3F Fogarty catheter inflated to tension was performed over a 6cm segment of the abdominal aorta distal to the renal arteries using fluoroscopic guidance. Balloon injury and imaging were performed under general anesthesia using ketamine 45mg/kg and xylazine 5.5mg/kg for induction and maintenance with inhaled 2% isoflurane.

Synthesis of CLIO-CyAm7, a NIR fluorescent ultrasmall superparamagnetic iron oxide nanoparticle. Crosslinked iron oxide (CLIO) nanoparticles were obtained from the Center for Systems Biology Chemistry Core at Massachusetts General Hospital (Supplemental Figure 2). Into 400 µL of dimethylsulfoxide, 2 mg of the NIR fluorophore CyAm7 (λ_{max} absorption = 744 nm, λ_{max} emission = 769 nm) was dissolved and added to 40 mg of CLIO (9.98 mg Fe/mL in PBS). The reaction was allowed to proceed for 16 hours, at which time it was filtered through Sephadex G25 to yield the conjugate (CLIO-CyAm7, 5.0 mg Fe/mL, 1.4×10^{-4} M CyAm7).

CLIO-CyAm7 deposition in atherosclerosis and atherothrombosis protocol. Ten weeks after balloon injury, CLIO-CyAm7 (2.5 mg Fe/kg, n=21) or saline (n=3) was

injected intravenously. At twenty-four hours, 9 rabbits were sacrificed for histological assessment and 15 rabbits underwent pharmacologic triggering to induce plaque thrombosis. For pharmacologic triggering, Russell's viper venom (0.15 mg/kg IP, Sigma Chemical Co) followed 30 minutes later by histamine (0.02 mg/kg IV, Sigma Chemical Co) were injected twice at a 24-hour interval.[1, 2] Rabbits were imaged pre-trigger (angiography, 2D NIRF imaging, intravascular ultrasound (IVUS)) and 48-hours post-trigger (angiography, IVUS). Rabbits were then sacrificed and perfused with saline.

In vivo intra-arterial NIRF molecular Imaging and IVUS structural imaging

NIRF imaging of atheroma cellularity. Custom-built standalone 2D NIRF catheter-based system utilizes continuous wave NIR fiber-coupled laser with excitation light of 750nm.[3] The NIRF fiber was placed percutaneously through the carotid artery into the rabbit aorta under fluoroscopic guidance. The fiber was mechanically rotated and retracted to produce a 2D image of the vessel wall (MATLAB R2011a MathWorks). Four 90-100cm pullbacks from the iliac bifurcation to the renal arteries were performed, with two different placements of the guidewire. NIRF imaging was performed through blood, without flushing, as light penetrates efficiently in the NIR window.[4]

2D NIRF signal analysis. The raw NIRF signal was filtered using a low pass filter and background subtraction. The signal was then averaged over 3 mm segments along the length of the aorta (MATLAB).[3] The maximum signal in a 3 mm segment along multiple pullbacks was calculated (Supplemental Figure 3). Signal from vessels of diameter greater than 5 mm on IVUS due to aneurysm formation were excluded from NIRF analysis given the high degree of NIR light attenuation in larger diameter vessels. NIRF images were quantified using target-to-background ratio (TBR), defined as the signal from an area of plaque divided by the signal from a normal, uninjured segment of the

aorta. The length of the aorta was divided into six 1.5 cm segments and correlated with *ex vivo* imaging and histology for analysis. The maximal TBR from all pullbacks in each segment was calculated (MATLAB). Segments were characterized as either plaque or normal vessel based on neointimal thickening on pre-trigger IVUS imaging or microscopy.

IVUS Structural assessment of atherosclerosis and atherothrombosis. IVUS imaging (Galaxy IVUS System, Boston scientific, Natick, MA) was performed pre- and post-pharmacologic thrombus triggering. One rabbit did not undergo IVUS post-trigger imaging due to technical difficulties. IVUS was co-registered with NIRF imaging using fluoroscopy of the radiopaque marker at the end of the IVUS catheter before and after imaging. Pre- and post-IVUS images were co-registered to each other using side branches as fiducials. Thrombi were identified on cross-sectional post-trigger IVUS imaging as new luminal defects. IVUS images were further reconstructed into 6 long axis images for additional visualization of luminal thrombi and comparison to NIRF imaging (MATLAB). The vessel diameter was calculated as the average diameter along two perpendicular planes on cross sectional images.

Endothelial permeability studies. The relationship between CLIO-CyAm7 nanoparticle deposition and impaired endothelial permeability was assessed by Evans Blue dye leakage[5] in a separate cohort of rabbits (n=7) who were intravenously injected with Evans Blue (6 mL 0.5%, Sigma Chemical Co) 30 minutes prior to sacrifice.[5] A higher dose of CLIO-CyAm7 (5.0 mg/kg IV 24 hours prior to sacrifice) was used to overcome fluorescence overlap with Evans Blue.

Fluorescence Reflectance Imaging (FRI)

After sacrifice, FRI was performed to image CLIO-CyAm7 fluorescence signal along the length of the aorta (Kodak Carestream 4000 MMPro). For FRI, the resected aorta was elongated to the *in vivo* length determined by angiography and imaged in NIR (excitation 716 to 756 nm, emission 780 to 820 nm, 16 seconds) and white light. The target signal for analysis was defined as a 3 cm area of atheroma manually traced in the area of balloon injury (ImageJ, NIH, Bethesda MD). The background noise was measured in an adjacent image region measuring the same area as the target region. The uninjured renal artery was utilized as a control vessel. For FRI imaging, the renal artery was selected as the preferred control segment as it was not instrumented at all during the initial balloon injury with sheath, guidewire or Fogarty balloon delivery. As the renal artery was too small for in vivo imaging, the larger uninjured aorta was used as the control vessel for in vivo imaging and the corresponding microscopy. The signal-to-noise ratio (SNR) was calculated for all non-triggered rabbits (n=6) as the target atheroma signal divided by the standard deviation of background noise.[3] The target-to-background ratio (TBR) was defined as the target atheroma signal divided by the signal from the control uninjured renal artery.

Histological Assessment of CLIO-CyAm7 and Atherothrombosis

Histology, immunofluorescence (IF), and immunohistochemistry (IHC). Resected aortas were elongated to *in vivo* length as determined by presacrifice angiography, systematically divided into 1.5 cm segments and marked with tissue marking ink for co-registration. Then, 0.5 cm segments were embedded in OCT (Sakura, Finetek, Torrance, CA), flash frozen, and cryosectioned (6μm). Sections were stained using Carstairs' stain to assess general morphology and collagen structure (blue) and to identify fibrin rich thrombi (red). Adjacent sections were stained by IF and IHC using the antibodies RAM11 for macrophages, CD31 for endothelial cells, and α-smooth muscle actin (aSMA)

for SMCs.

Immunohistochemistry (IHC) and immunofluorescence (IF) antibodies used for staining: RAM11 for macrophages (Dako, IF 1:200, IHC 1:500), CD31 for endothelial cells (Abcam, IF 1:200, IHC 1:100), and α-smooth muscle actin (aSMA) for SMCs (Abcam, IF 1:200, IHC 1:100). All stains were performed on an uninjured renal artery section for controls. For IF, secondary goat anti-mouse Texas Red antibody (1:200 dilution, Abcam) was used. RAM11 IHC was incubated with secondary anti-mouse Alkaline Phosphatase-conjugated antibody, stained using Vulcan fast red chromagen (Biocare medical). CD31 and aSMA IHC used biotin-streptavidin conjugation for visualization. All IHC sections were counterstained with hematoxylin.

Fluorescence microscopy of CLIO-CyAm7 deposition in atheroma. CLIO-CyAm7 was visualized on histological sections using customized NIR filters (Eclipse 90i, Nikon Instruments, ex/em: 710/810 nm, 500 ms exposure). The fluorescence distribution of Evans blue and secondary antibodies (RAM11, CD31, and aSMA) were imaged using a Texas Red filter (ex/em 590/620 nm, 100ms exposure). Autofluorescence (ex/em 480/535 nm; 500 ms exposure) was measured during all FM studies. Epifluorescence microscopy images were acquired at 40x magnification.

CLIO-CyAm7 microscopic accumulation was analyzed on FM at 0.5 cm intervals along the aorta (n=183 sections). Of the 183 microscopy sections analyzed, each section was classified as plaque (n=144) or normal (n=39), based on the presence of intimal thickening on autofluorescence-based microscopy. Each atheroma section was further defined as thrombosed (n=38) or non-thrombosed (n=106) based on Carstairs' stain evidence of adherent fibrin-rich thrombi. For quantitative fluorescence analysis, an FM

image of the entire plaque was obtained from unstained, non-coverslipped sections at 10x magnification. A signal intensity threshold was determined visually to limit background NIR fluorescence and applied equally to all images. After thresholding, a region of interest (ROI) to analyze superficial intimal CLIO-CyAm7 signal was defined as all tissue within 100 μm of the luminal edge. One section from each 0.5 cm segment of aorta was analyzed using this method, and the maximum percent positive area of three sections across a 1.5 cm segment (previously demarcated with tissue marking ink to correspond with *in vivo* imaging) was used for further analysis of each segment (normal vessel n=25; atheroma without thrombus, n=30; atheroma with adherent thrombus, n=21). All analyses were performed using ImageJ (NIH, Bethesda, MD).

Statistical Analysis

Statistical analyses were completed using GraphPad Prism (v5.0 GraphPadSoftware, San Diego, CA). Appropriate threshold for specificity and sensitivity calculations were determined using an ROC curve for optimization. For all 2D NIRF TBR and microscopy analyses between two groups, the nonparametric Mann-Whitney U test was used. Data is presented as mean ± standard deviation.

References

1. Phinikaridou A, Hallock KJ, Qiao Y, Hamilton JA. A robust rabbit model of human atherosclerosis and atherothrombosis. *Journal of lipid research*. 2009;50:787-797
2. Phinikaridou A, Ruberg FL, Hallock KJ, Qiao Y, Hua N, Viereck J, Hamilton JA. In vivo detection of vulnerable atherosclerotic plaque by MRI in a rabbit model. *Circulation. Cardiovascular imaging*. 2010;3:323-332
3. Jaffer FA, Calfon MA, Rosenthal A, Mallas G, Razansky RN, Mauskapf A, Weissleder R, Libby P, Ntziachristos V. Two-dimensional intravascular near-infrared fluorescence molecular imaging of inflammation in atherosclerosis and stent-induced vascular injury. *Journal of the American College of Cardiology*. 2011;57:2516-2526
4. Osborn EA, Jaffer FA. The year in molecular imaging. *JACC. Cardiovascular imaging*. 2010;3:1181-1195

5. Phinikaridou A, Andia ME, Protti A, Indermuehle A, Shah A, Smith A, Warley A, Botnar RM. Noninvasive magnetic resonance imaging evaluation of endothelial permeability in murine atherosclerosis using an albumin-binding contrast agent. *Circulation*. 2012;126:707-719

Supplemental Figure Legends

Supplemental Figure 1. Rabbit atherothrombosis protocol. Schematic of timeline for rabbit triggered thrombosis. Alternating 1% high cholesterol diet (HCD) with normal chow diet starting two weeks prior to aortic balloon injury. After completion of the twelve-week diet protocol, rabbits underwent pharmacologic triggering and in vivo survival imaging with near infrared fluorescence (NIRF) and intravascular ultrasound (IVUS) imaging. Pharmacologic triggering, with Russell's viper venom followed by histamine injections, occurred twice, twenty-four hours apart. At forty-eight hours after initial triggering, in vivo IVUS imaging was performed followed by sacrifice and ex vivo studies.

Supplemental Figure 2. Schematic of CLIO-CyAm7 nanoparticle. Representation of the synthesized CLIO-CyAm7 particle with an ultrasmall paramagnetic iron oxide (USPIO) nanoparticle core conjugated to an NIR fluorophore CyAm7.

Supplemental Figure 3. Example analysis of in vivo NIRF imaging in a single rabbit. Due to distance-dependent attenuation of NIRF signal, imaging pullbacks were repeated four times to account for the variation in placement of the catheter in relation to the arterial wall. (A) Four pullbacks were aligned using the radiopaque catheter tip under fluoroscopy and the maximum TBR was calculated along 360 degrees for 3 mm segments. Each pullback was graphed in a different color. (B) The maximum TBR was identified from all pullbacks along the length of the aorta and used for further analysis.

Supplemental Figure 4. Receiver operator curve (ROC) for fluorescence microscopy. (A,B) Histogram of values for fluorescence microscopy percent positive CLIO CyAm7 pixels represented linearly and on a logarithmic scale. (C) ROC curve of

sensitivity and specificity for determination of optimal threshold of percent positive area. The optimal threshold was determined to be 0.85% positive pixels, which represents a likelihood ratio of 2.16.

Supplemental Figure 1:

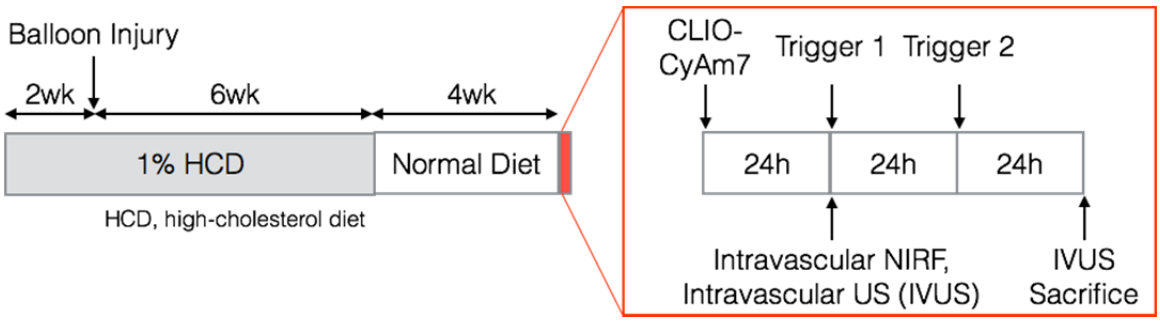

Supplemental Figure 2:

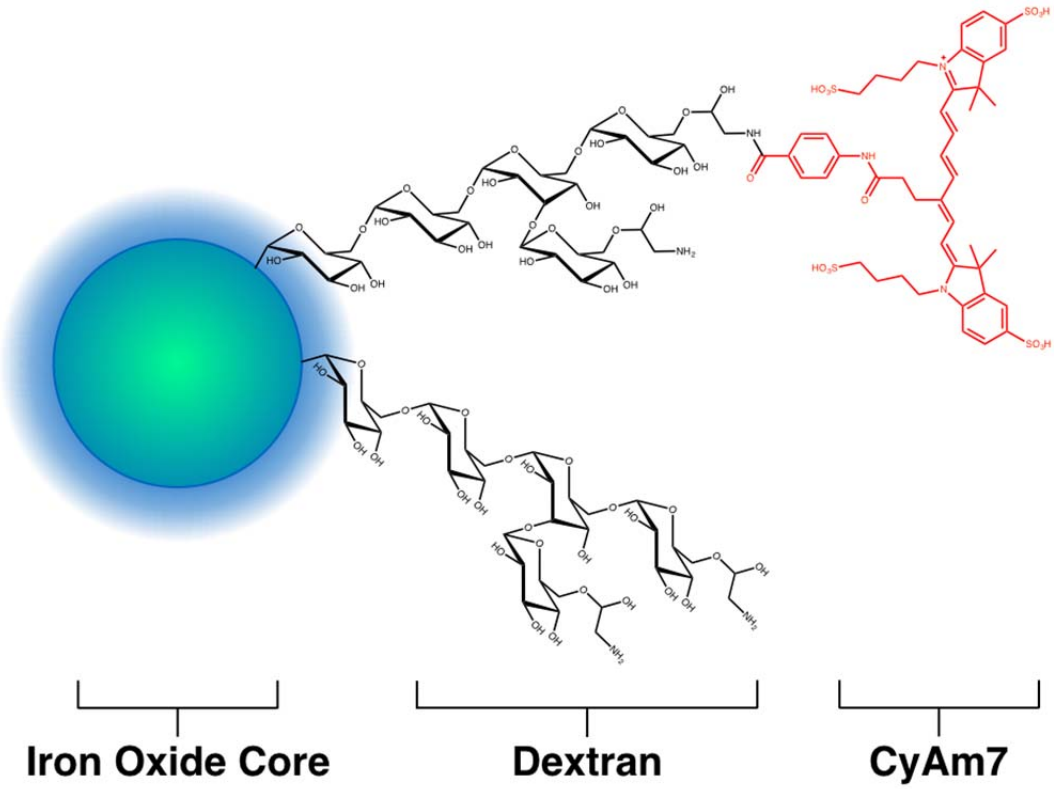

Supplemental Figure 3:

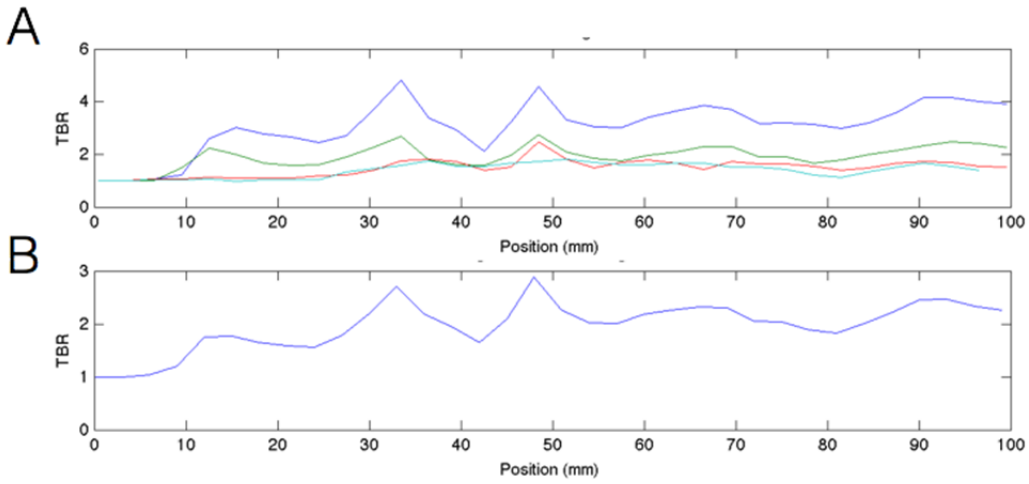

Supplemental Figure 4